Baseline-free damage localization of wind turbine towers using optimal fractional-order curvature ratio curve: A two-step validation approach

Baseline-free damage localization of wind turbine towers using optimal fractional-order curvature ratio curve: a two-step validation approach

Yuanqing Fan[1,2], Yang Yang[1,2,*], Zhewei Wang[1,2], Giuseppe Lacidogna[3], Jie Luo[4], Jiaji Wang[5]

[1] School of Civil Engineering, Chongqing University, Chongqing, China

[2] Institute for Liyang Smart City, Chongqing University, Jiangsu, China

[3] Department of Structural, Geotechnical and Building Engineering, Politecnico di Torino, 10129 Torino, Italy

[4] Guizhou Investment and Construction Co.,Ltd. Of China State Construction Fourth Engineering Division Corp., Ltd., Guizhou, China

[5] Department of Civil Engineering, The University of Hong Kong, Hong Kong, China

Abstract

Wind turbine towers play a vital role in supporting turbines and ensuring the stability and efficiency of power generation. However, long-term exposure to complex environmental and operational loads makes them vulnerable to local stiffness degradation. This study proposes a baseline-free damage localization method based on an optimal fractional-order curvature ratio curve (OFCRC), which enables the identification of damage locations using a single measurement without requiring reference data from the intact state. In the first stage, the OFCRC is derived and employed as a sensitive curvature-based indicator to detect abrupt stiffness variations, enabling rapid and accurate localization of potential damage. The OFCRC is constructed directly from the ratios of relative displacement statistical moments between adjacent measuring points, without solving any eigenvalue problem or extracting mode shapes, and thus constitutes a fully self-contained baseline-free localization indicator. In the second stage, to verify and quantify the detected damage, the identified mode shapes—obtained through the team's existing optimal fractional statistical moment (FSM) approach—are incorporated into an improved direct stiffness method (IDSM) for evaluating the extent of stiffness loss. Numerical simulations, scaled-model tower experiments, and field measurements of a 2 MW wind turbine tower validate the method's effectiveness. The proposed OFCRC method represents the novel contribution of this study, enabling rapid and baseline-free localization, while the subsequent integration with established FSM–IDSM methods provides a complete two-step framework for both localization and quantification. The proposed

* Corresponding authors.

Email address: yangyangcqu@cqu.edu.cn (Yang Yang)

approach provides a robust, baseline-free, and single-measurement solution for the rapid structural health screening of wind turbine tower groups.

Keywords: fractional order statistical moments, wind turbine tower, modal identification, damage identification, baseline-free

1. Introduction

With the rapid global energy structural transformation and green low-carbon development, wind energy, as a clean and renewable energy source, is gradually becoming an important component of energy strategies in various countries [1][2][3]. As a clean and renewable resource, wind energy has seen substantial growth in installed capacity and power generation, making significant contributions to alleviating energy pressure and reducing greenhouse gas emissions [4][5]. However, the increasing scale of wind farms and extended operational periods have posed significant challenges to wind turbine towers, which serves as the key supporting structures for wind turbines [6][7]. Wind turbine towers are exposed to complex and dynamic natural environments for a long time, such as extreme weather and geological changes, while also bearing significant loads from turbine operation [8][9]. These factors contribute to various forms of damage to the towers over time [10][11]. Such damage not only compromises the load-bearing capacity and stability of the wind turbine tower but may also causes accidents, posing a serious threat to the normal operation of the wind farm and personnel safety [12]. Therefore, timely and accurate detection, localization, and quantitative analysis of damage to wind power towers are of great significance for ensuring operational safety, extending service life, and reducing maintenance costs [13][14][15].

Traditional damage detection methods, such as visual inspection and tapping tests, suffer from low detection efficiency and limited accuracy, making them hard to meet the needs of large-scale wind farms [16][17][18]. Recent advancements in sensor technology, signal processing technology, and artificial intelligence technology have led to the development of innovative damage identification methods [19][20][21]. Ren et al. proposed a method for estimating expected fatigue damage in wind turbines by an efficient active learning Kriging approach named ALK-EFDA. This method was validated with a 15 MW Semi-submersible floating wind turbine model [22]. Guo et al. proposed an unsupervised statistical estimation method to detect wind turbine tower damage. The proposed method has demonstrated better robustness and higher computational efficiency with a 5 MW monopile OWT by OpenFAST and field test data by combining environmental variables clustering analysis and interval correlation [23]. Xiong et al. established a 180m lattice wind turbine support structure which is prefabricated and assembled mainly from thin-walled circular hollow steel tube elements and proposed a new integrated multi-scale fatigue assessment method to address the shortcomings of the equivalent fatigue load method commonly used in engineering design [24]. Li et al. proposed a damage index based on acceleration response and developed a real-time monitoring system to address the issue of most concrete pipe sections in wind turbine towers requiring shutdown work. The reliability of the proposed method was verified through experimental research and parameter analysis [25]. Bai et al. designed a residual neural network-assisted fatigue estimation method and proposed a probabilistic fatigue analysis framework based on numerical simulation to estimate the fatigue damage of wind turbine towers, which can significantly improve the efficiency of the proposed probabilistic fatigue analysis method [26]. Zhang et al. determined the objective function based on modal intrinsic properties and modal curvature and established a finite element model of a 5MW single-pile wind turbine using ANSYS. The proposed two-step method can identify the location and severity of structural damage separately, improving the efficiency of on-site testing [27]. Hubbard et al. evaluated and compared two distributed fiber optic sensing technologies based on Rayleigh (optical frequency domain reflectometry and phase-based optical time domain reflectometry) to assess their ability and scope of use in monitoring the dynamic structural behavior of wind turbine towers under free and forced vibrations [28]. Motlagh et al. established a finite element model based on NREL 5MW reference onshore wind turbine and proposed a multi-layer two-dimensional wavelet decomposition method to identify damage locations in wind turbine towers with and without soil structure interactions [29].

Among vibration-based damage identification approaches, eigenvalue perturbation methods, including higher-order formulations, constitute a well-established analytical framework for structural health monitoring [33][33][33]. These methods relate variations in eigenvalues and eigenvectors (e.g., natural frequencies and mode shapes) to changes in structural parameters through sensitivity analysis, enabling the inverse estimation of damage location and severity. Owing to their analytical formulation and computational efficiency, such approaches are, in principle, well suited for continuous or real-time monitoring when reliable baseline modal data are available [33][33]. However, their practical application to rapid initial health screening of wind turbine towers is constrained by several inherent limitations. First, an accurate baseline model or reference measurement from the intact state is generally required, as the identification process relies on differences between damaged and undamaged configurations [33][33]. For many in-service wind turbine towers lacking historical baseline data, this requirement is often difficult to satisfy. Second, the reliability and stability of the solution typically depend on the identification of multiple higher-order modes, which remains challenging for large-scale, flexible tower structures under ambient excitation and limited sensor deployment [33][33].

These inherent limitations highlight that most current damage detection methods for wind turbine tower structures still require analyzing dynamic response signals before and after structural damage [33], or at least depend on a reliable baseline. For the rapid initial health screening of wind turbine towers, traditional methods therefore face challenges such as high time and labor demands, high cost, operational complexity, and potential human factors [33][33]. In summary, while extensive research has been conducted on damage identification of wind turbine tower structures, relatively little attention has been paid to baseline-free methods that enable rapid initial screening based on a single measurement. A baseline-free approach is urgently needed to overcome these limitations.

To address these limitations, this study proposes a novel baseline-free damage localization method based on the optimal fractional-order curvature ratio curve (OFCRC). Derived from fractional calculus theory, the OFCRC captures subtle curvature variations between adjacent measurement points and enables the identification of stiffness mutations through characteristic abrupt changes in the curve. The proposed method requires only a single measurement and does not rely on reference data from the intact state, making it particularly suitable for rapid damage screening of large-scale wind turbine towers. This constitutes the first stage of the proposed framework and represents the core innovation of this study. The OFCRC alone serves as a self-contained damage screening tool, requiring neither baseline data nor prior modal identification.

Furthermore, to verify and quantify the identified damage, the OFCRC-based localization is integrated with the fractional statistical moment (FSM)-based modal identification method [34] and the improved direct stiffness method (IDSM) [40], both of which have been validated in previous studies. This integration forms a two-stage, baseline-free framework capable of identifying both the location and severity of structural damage. The effectiveness and robustness of the proposed approach are demonstrated through numerical simulations and field experiments on wind turbine towers. Notably, the proposed framework is not intended to replace real-time monitoring approaches such as eigenvalue perturbation methods, but rather to provide a complementary solution for rapid, baseline-free initial damage screening in practical engineering applications.

2. Theoretical derivation

2.1 Derivation of the fractional-order curvature ratio curve (OFCRC)

The fractional-order curvature ratio curve (OFCRC) is introduced as a baseline-free index for damage localization in wind turbine tower structures. When a multi-degree-of-freedom system structure is excited by ground acceleration $\ddot{x}_g(t)$, its motion equation is:

$$\boldsymbol{M}\ddot{\boldsymbol{X}}(t) + \boldsymbol{C}\dot{\boldsymbol{X}}(t) + \boldsymbol{K}\boldsymbol{X}(t) = \boldsymbol{P}(t) = -\boldsymbol{M}\boldsymbol{I}\ddot{x}_g(t) \tag{1}$$

In Eq. (1), $\boldsymbol{M}, \boldsymbol{C}, \boldsymbol{K}, \ddot{\boldsymbol{X}}(t), \dot{\boldsymbol{X}}(t), \boldsymbol{X}(t)$ represent the mass matrix, damping matrix, stiffness matrix, acceleration response, velocity response, and displacement response, respectively. $\boldsymbol{P}(t)$ represents motivation. $\boldsymbol{I}$ is the unit column vector. According to the orthogonality of the vibration modes, when the structure is Rayleigh damped, the motion equation of the structural vibration mode response can be obtained:

$$\ddot{Y}_n(t) + 2\xi_n\omega_n\dot{Y}_n(t) + \omega_n^2 Y_n(t) = \frac{P_n(t)}{M_n} \quad n = 1,2,\dots,N \tag{2}$$

In Eq. (2), $Y_n(t)$ is the generalized coordinate corresponding to the n-th mode of vibration, while M_n, N, ξ_n, ω_n are the n-th generalized mass, degrees of freedom, n-th damping ratio, and n-th circular frequency of the structure, respectively. $P_n(t)$ is the generalized force corresponding to the n-th mode of vibration. The solved modal response is:

$$Y_n(t) = \int_0^t P_n(t)h_n(t-\tau)d\tau \tag{3}$$

$$\begin{gathered} h_n(t) = \frac{1}{M_n\omega_{Dn}} exp[-\xi_n\omega_n(t-\tau)]sin\omega_{Dn}t \\ \omega_{Dn} = \omega_n(1-\xi_n^2)^{1/2} \end{gathered} \tag{4}$$

Based on the mode superposition method, the displacement response $z_i(t)$ of the i-th measuring point of the structure can be expressed as:

$$z_i(t) = \sum_{n=1}^{N} B_n Y_n(t) = \sum_{n=1}^{N} \phi_n^i\, Y_n(t) \tag{5}$$

In Eq. (5), ϕ_n^i represents the value of the n-th mode of vibration of the structure at the i-th measurement point. Under steady excitation conditions, the response process of the linear elastic structure will also be stationary, and its autocorrelation function is:

$$R_{zi}(\tau) = E[z_i(t)z_i(t+\tau)] = E\left[\sum_{m=1}^{N}\sum_{n=1}^{N} B_m\, B_n Y_m(t) Y_n(t+\tau)\right] \tag{6}$$

Substitute Eq. (3) into Eq. (6) to simplify and solve the displacement response autocorrelation function of the i-th measuring point:

$$R_{zi}(\tau) = \sum_{m=1}^{N} \sum_{n=1}^{N} \iint_{0}^{\infty} B_m B_n R_{p_m P_n}(\tau - u_2 + u_1) h_m(u_1) h_n(u_2) du_1 du_2 \tag{7}$$

In Eq. (7), $R_{p_m P_n}$ represents the covariance function of the excitation $P_m(t)$ and $P_n(\tau + t)$. By performing the Fourier transform on the autocorrelation function $R_{zi}(\tau)$ of the displacement response at the i-th measuring point, the power spectral function of the displacement response at the i-th measuring point can be obtained:

$$S_{zi}(\omega) = \frac{1}{2\pi} \int_{-\infty}^{+\infty} R_{zi}(\tau) \exp(-i\omega\tau) d\tau \tag{8}$$

Substituting Eq. (7) into Eq. (8) can solve the displacement response power spectral density function of the i-th measuring point:

$$S_{zi}(\omega) = \sum_{m=1}^{N} \sum_{n=1}^{N} B_m B_n \, H_m(-i\omega) H_n(i\omega) S_{p_m P_n}(\omega) \tag{9}$$

In Eq. (9), $S_{p_m P_n}(\omega)$ represents the mutual power spectral density function of excited $P_m(t)$ and $P_n(\tau + t)$, and has:

$$\begin{aligned} H_m(-i\omega) &= \frac{1}{K_m[1 - 2i\xi_m(\omega/\omega_n) - (\omega/\omega_n)^2]} \\ H_n(i\omega) &= \frac{1}{K_n[1 - 2i\xi_n(\omega/\omega_n) - (\omega/\omega_n)^2]} \end{aligned} \tag{10}$$

In Eq. (10), $K_m = \boldsymbol{\phi_m^T K \phi_m}$ and $K_n = \boldsymbol{\phi_n^T K \phi_n}$ represent the m-th and n-th order generalized stiffness of the structure, respectively. For small damping systems, the cross term in Eq. (9) contributes very little to the structural response. In this case, Eq. (9) can be simplified as:

$$S_{zi}(\omega) = \sum_{n=1}^{N} {B_n}^2 |H_n(i\omega)|^2 S_{p_n P_n}(\omega) \tag{11}$$

In Eq. (11), $S_{p_n P_n}(\omega)$ represents the self-power spectral density function that excites $P_n(t)$. When the surface excitation acceleration $\ddot{x}_g(t)$ follows a Gaussian distribution with a mean of zero, and its self-power spectral function is a constant S_0, then the self-power spectral density function $P_n(t)$ of the external load $S_{P_n P_n}(\omega)$ can be expressed as:

$$S_{p_n P_n}(\omega) = \boldsymbol{\phi}_n^T \boldsymbol{M I I}^T \boldsymbol{M}^T \boldsymbol{\phi}_n S_0 \tag{12}$$

By substituting Eqs. (10) and (12) into Eq. (11), the displacement response power spectral density function $S_{zi}(\omega)$ of the i-th measuring point can be calculated. By using the relationship between the standard deviation and the response power spectral density function, the *j*-th order 32/7th order displacement statistical moment of the *i*-th measuring point can be obtained (The specific fractional order 32/7 is adopted as the optimal FSM, as demonstrated in [34], due to its enhanced sensitivity to structural damage while maintaining robustness against measurement noise):

$$M_{i,j}^{\frac{32}{7}}(d) = \frac{\Gamma(\frac{39}{14})}{\sqrt{\pi}} \left[\pi \frac{\boldsymbol{\phi}_j^T \boldsymbol{M} \boldsymbol{I} \boldsymbol{I}^T \boldsymbol{M}^T \boldsymbol{\phi}_j S_0}{M_j^2 \omega_j^3 \xi_j} (\phi_{i,j})^2 \right]^{\frac{16}{7}} \tag{13}$$

Among them, Γ is the Gamma function, and $M_{i,j}^{\frac{32}{7}}(d)$ is the *j*-th order displacement statistical moment of the *i*-th measuring point. Similarly, the *j*-th order 32/7th order displacement statistical moment of the (*i* +1)-th measuring point can be calculated, and the ratio of the statistical moments of two adjacent measuring points can be obtained:

$$M_{i,j}^{32/7}(d) / M_{i+1,j}^{32/7}(d) = (\phi_{i,j})^{\frac{32}{7}} / (\phi_{i+1,j})^{\frac{32}{7}} \tag{14}$$

When the inherent parameters of the structure are determined, the ratio of the vibration modes of adjacent measuring points should be constant. From Eq. (14), it can be seen that the ratio of the vibration modes of adjacent measuring points is the statistical moment ratio. The ratio of the *j*-th order statistical moment between the *i*-th measurement point and the (*i* +1)-th measurement point is defined as $T_{i,i+1}^{j}$. If the mode shape value of measurement point 1 is set as the reference point, the mode shape vector $\Phi_j^{\frac{32}{7}}$ can be calculated as follows:

$$\Phi_j^{\frac{32}{7}} = \left[\phi_{1,j}^{\frac{32}{7}}, \sqrt[\frac{32}{7}]{T_{1,2}^{j}} \phi_{1,j}^{\frac{32}{7}}, \cdots, \sqrt[\frac{32}{7}]{T_{i,i+1}^{j}} \phi_{i,j}^{\frac{32}{7}}, \cdots, \sqrt[\frac{32}{7}]{T_{m-1,m}^{j}} \phi_{m-1,j}^{\frac{32}{7}} \right], m = 1,2, \ldots \tag{15}$$

In Eq. (15), $\phi_{i,j}^{\frac{32}{7}}$ represents the *j*-th order 32/7th order vibration mode value of the *i*-th measuring point. Through the above derivation, the structural modal shape can be solved by using the 32/7th order displacement statistical moment.

Considering that the first-order mode is easy to measure and relatively accurate in actual testing, the following derivations are based on the first-order mode as an example. The relative displacement statistical moment of the *i*-th measuring point at order 32/7, denoted as $M_i^{\frac{32}{7}}(d_{rel})$ (i.e., the relative displacement statistical moment of the *i*-th measuring point at order 32/7 to the (*i* -1)-th measuring point), can be expressed as:

$$M_i^{\frac{32}{7}}(d_{rel}) = \Gamma(\frac{39}{14})\pi^{\frac{25}{14}}[\frac{\boldsymbol{\phi}_1^T \boldsymbol{M}\boldsymbol{I}\boldsymbol{I}^T\boldsymbol{M}^T\boldsymbol{\phi}_1 S_0}{M_1^2\omega_1^3\xi_1}(\phi_{1,i} - \phi_{1,i-1})^2]^{\frac{16}{7}} \tag{16}$$

-Similarly, the displacement statistical moment $M_{i+1}^{\frac{32}{7}}(d_{rel})$ of the (i +1)-th measuring point relative to the i-th measuring point can be obtained, and the ratio of adjacent measuring points can be expressed as:

$$\frac{M_i^{\frac{32}{7}}(d_{rel})}{M_{i+1}^{\frac{32}{7}}(d_{rel})} = \frac{(\phi_{1,i} - \phi_{1,i-1})^{\frac{32}{7}}}{(\phi_{1,i+1} - \phi_{1,i})^{\frac{32}{7}}} \tag{17}$$

For the wind turbine tower structure model that can be approximated and simplified as a cantilever beam, the expression of the first-order bending vibration mode of the structure under initial conditions can be obtained [41]:

$$\phi_1(x) = A_1[\cosh ax - \cos ax + \frac{\cos aL + \cosh aL}{\sin aL + \sinh aL}(\sin ax - \sinh ax)] \tag{18}$$

In Eq. (16), A_1 is a non-zero constant and $aL = 1.875$. In field measurements, assuming the distance between adjacent measurement points is h and the height of the i-th measurement point is y, the FSM ratio at the y position of the measurement point is:

$$\frac{M_i^{\frac{32}{7}}(d_{rel})}{M_{i+1}^{\frac{32}{7}}(d_{rel})} = \frac{[\phi_1(y) - \phi_1(y-h)]^{\frac{32}{7}}}{[\phi_1(y+h) - \phi_1(y)]^{\frac{32}{7}}} \tag{19}$$

By substituting Eq. (18) into Eq. (19) and taking the derivative of the height y of the measuring point, we can obtain:

$$\begin{aligned} \left(M_i^{\frac{32}{7}}(d_{rel}) \Big/ M_{i+1}^{\frac{32}{7}}(d_{rel}) \right)' \\ = C\{\frac{32}{7}[\phi_1'(y) - \phi_1'(y-h)]^{\frac{25}{7}} * [\phi_1(y+h) - \phi_1(y)] \\ - \frac{32}{7}[\phi_1'(y+h) - \phi_1'(y)]^{\frac{25}{7}} * [\phi_1(y) - \phi_1(y-h)]\} \end{aligned} \tag{20}$$

In Eq. (20), $C > 0$ always holds under the condition of $y \in (h, l-h)$, which means that when the lateral stiffness of the wind turbine tower structure remains unchanged, the FSM ratio curve of adjacent lower and upper measurement points shows a smooth and continuous increasing trend with the increase of measurement point height.

$$\begin{aligned} \boldsymbol{M} = \boldsymbol{M_0} + \varepsilon \boldsymbol{M_1} \\ \boldsymbol{K} = \boldsymbol{K_0} + \varepsilon \boldsymbol{K_1} \end{aligned} \tag{21}$$

In Eq. (21), $\boldsymbol{M_0}, \boldsymbol{K_0}$ are the mass matrix and stiffness matrix corresponding to the original system, ε is the damage parameter, and when $\varepsilon = 0$, it is the original system. $\varepsilon \boldsymbol{M_1}$ and $\varepsilon \boldsymbol{K_1}$ represent the changes in the mass matrix and stiffness matrix, respectively. Solving the structural eigenvalue problem can be expressed as:

$$\boldsymbol{K\phi_n} = \lambda_n \boldsymbol{M\phi_n} = \omega_n^2 \boldsymbol{M\phi_n} \tag{22}$$

In Eq. (22), $\boldsymbol{\phi_n}$ is the n-th order mode vector, and $\lambda_n = \omega_n^2$ is the square of the n-th order circular frequency. When the quality matrix and stiffness matrix change, that is, when $\varepsilon \boldsymbol{M_1}$ and $\varepsilon \boldsymbol{K_1}$ change, the eigenvalues and eigenvectors will change. According to the perturbation method, by expanding $\boldsymbol{\phi_n}$ and λ_n into a power series with ε, we can obtain:

$$\begin{gathered} \lambda_n = \lambda_{0n} + \varepsilon\lambda_{1n} + \varepsilon^2\lambda_{2n} + \cdots \\ \boldsymbol{\phi}_n = \boldsymbol{\phi}_{0n} + \varepsilon\boldsymbol{\phi}_{1n} + \varepsilon^2\boldsymbol{\phi}_{2n} + \cdots \end{gathered} \tag{23}$$

In Eq. (23), λ_{0n} and $\boldsymbol{\phi}_{0n}$ are the eigenvalues and eigenvectors of the original system, λ_{1n} and $\boldsymbol{\phi}_{1n}$ are the first-order perturbations of the eigenvalues and eigenvectors, and λ_{2n} and $\boldsymbol{\phi}_{2n}$ are the second-order perturbations of the eigenvalues and eigenvectors, respectively. When the lateral stiffness of the structure changes and the mass matrix remains unchanged, the first-order perturbation value can be expressed as:

$$\begin{gathered} \lambda_{1n} = \boldsymbol{\phi}_{0n}^T K_1 \boldsymbol{\phi}_{0n} \\ \boldsymbol{\phi}_{1n} = \sum_{j=1, j\neq n}^{N} \frac{1}{\lambda_{0n} - \lambda_{0j}} \boldsymbol{\phi}_{0j}^T K_1 \boldsymbol{\phi}_{0n} \boldsymbol{\phi}_{0j} \end{gathered} \tag{24}$$

When the lateral stiffness of the m-th section of the wind turbine tower structure (between measurement point m and measurement point $m-1$) changes, it can be obtained that:

$$\varepsilon \boldsymbol{K_1} = \begin{bmatrix} 0 & \cdots & 0 & 0 & \cdots & 0 \\ \vdots & \ddots & \vdots & \vdots & ⋰ & \vdots \\ 0 & \cdots & -k_m & -k_m & \cdots & 0 \\ 0 & \cdots & -k_m & -k_m & \cdots & 0 \\ \vdots & ⋰ & \vdots & \vdots & \ddots & \vdots \\ 0 & \cdots & 0 & 0 & \cdots & 0 \end{bmatrix} \tag{25}$$

By substituting Eqs. (24) and (25) into Eq. (23), we can solve for:

$$\boldsymbol{\phi}_n = \boldsymbol{\phi}_{0n} + \sum_{j=1, j\neq n}^{N} \frac{-\varepsilon}{\lambda_{0n} - \lambda_{0j}} [k_m(\phi_{0n}^m - \phi_{0n}^{m-1}) * (\phi_{0j}^m - \phi_{0j}^{m-1})] \boldsymbol{\phi}_{0j} \tag{26}$$

In Eq. (26), ϕ_{0n}^m represents the m-th element corresponding to the n-th mode of vibration of the original system. Substituting Eq. (26) into Eq. (19), the FSM ratio of the i-th measurement point can be expressed as:

$$\frac{M_i^{\frac{32}{7}}(d_{rel})}{M_{i+1}^{\frac{32}{7}}(d_{rel})} = \frac{\left[\left(\phi_{01}^{i}-\phi_{01}^{i-1}\right)-\varepsilon k_m \sum_{j=2}^{N} \frac{1}{\lambda_{01}-\lambda_{0j}}\left(\phi_{01}^{m}-\phi_{01}^{m-1}\right)\left(\phi_{0j}^{m}-\phi_{0j}^{m-1}\right)\left(\phi_{0j}^{i}-\phi_{0j}^{i-1}\right)\right]^{\frac{32}{7}}}{\left[\left(\phi_{01}^{i+1}-\phi_{01}^{i}\right)-\varepsilon k_m \sum_{j=2}^{N} \frac{1}{\lambda_{01}-\lambda_{0j}}\left(\phi_{01}^{m}-\phi_{01}^{m-1}\right)\left(\phi_{0j}^{m}-\phi_{0j}^{m-1}\right)\left(\phi_{0j}^{i+1}-\phi_{0j}^{i}\right)\right]^{\frac{32}{7}}} \tag{27}$$

When the lateral stiffness of the structure changes in the m-th segment, according to Eq. (13), the FSM of the i-th measuring point will change accordingly. Define Δ_i as the FSM change variable for measuring point i before and after a sudden change in structural stiffness, as follows:

$$\Delta_i = \frac{\left(\phi_1^{i}-\phi_1^{i-1}\right)^{\frac{32}{7}}}{\left(\phi_1^{i+1}-\phi_1^{i}\right)^{\frac{32}{7}}} - \frac{\left(\phi_{01}^{i}-\phi_{01}^{i-1}\right)^{\frac{32}{7}}}{\left(\phi_{01}^{i+1}-\phi_{01}^{i}\right)^{\frac{32}{7}}} \tag{28}$$

By substituting Eq. (27) into Eq. (28) for solution, we can obtain:

$$\Delta_i = U \sum_{j=2}^{N} \frac{\varepsilon k_m}{\lambda_{01}-\lambda_{0j}}\left(\phi_{01}^{m}-\phi_{01}^{m-1}\right)\left(\phi_{0j}^{m}-\phi_{0j}^{m-1}\right)\left[\left(\phi_{01}^{i}-\phi_{01}^{i-1}\right)\left(\phi_{0j}^{i+1}-\phi_{0j}^{i}\right)-\left(\phi_{01}^{i+1}-\phi_{01}^{i}\right)\left(\phi_{0j}^{i}-\phi_{0j}^{i-1}\right)\right] \tag{29}$$

In Eq. (29), U is a non-zero constant. When $m \neq i$, the change Δ_i approaches 0. When the m-th segment of the structural stiffness undergoes a sudden change and approaches measurement point i, i.e. $m \approx i$, the change Δ_i is non-zero. This means that when the structural lateral stiffness mutation m-th segment is not equal to the measurement point i, the change Δ_i approaches 0. When the structural lateral stiffness mutation m-th segment is close to the measurement point i, the change Δ_i changes significantly. By combining Eq. (20), it can be concluded that the FSM ratio curve only exhibits significant fluctuations at positions where stiffness undergoes sudden changes while maintaining a continuous smooth state at positions where stiffness does not undergo sudden changes.

2.2 Verification and Damage Quantification via FSM–IDSM

After the potential damage locations are identified using the optimal fractional-order curvature ratio curve (OFCRC) in Section 2.1, this section performs quantitative verification using the team's previously developed techniques: the fractional statistical moment (FSM)-based modal identification method and the improved direct stiffness method (IDSM). The FSM-based modal identification theory was originally proposed and validated in Yang et al. (2024) [39], where fractional-order statistical moments were introduced to improve modal recognition under noisy and incomplete measurements. The improved direct stiffness method (IDSM) employed here was proposed in Yang et al. (2022) [42] and further refined in Yang et al. (2022) [43]. It eliminates the subjective penalty functions used in traditional stiffness inversion and directly estimates the element bending stiffness from identified mode shapes.

Using the modal shapes identified by the theory in section 2.1, this method achieves higher accuracy and eliminates the influence of subjective factors. By assuming that the modal shapes vary uniformly and linearly within each element, and only considering the first-order modal shapes, we can obtain:

$$\begin{gathered} M_{i+1} = M_i - \int_{x_i}^{x_{i+1}} \omega_1^2 \rho A \phi_1(x)(x_{i+1} - x)dx + V_i(x_{i+1} - x_i) \\ V_{i+1} = V_i - \int_{x_i}^{x_{i+1}} \omega_1^2 \rho A \phi_1(x)dx \end{gathered} \tag{30}$$

In Eq. (30), the bending moment values at both ends of the i-th element are denoted as M_i and M_{i+1}, respectively. V_i and V_{i+1} represent the shear force values at both ends of the i-th element, respectively. $\omega_1, \rho, A, \phi_1(x)$ represent the first-order frequency, density, cross-sectional area, and the first-order mode value at position x, respectively.

$$EI_i = \frac{M_i}{\phi_i''} \tag{31}$$

In Eq. (31), EI_i is the bending stiffness of the i-th element, and ϕ_i'' is the modal curvature of the i-th element, which can be calculated using the center difference method.

In this study, the FSM–IDSM combination is not a new development, but rather serves as a verification and quantitative extension to the newly proposed OFCRC localization framework. The FSM-derived modal shapes provide the necessary input for the IDSM to compute the stiffness distribution along the tower. Therefore, the integration of FSM–IDSM with the proposed OFCRC method enables both baseline-free localization and quantitative stiffness evaluation, while maintaining computational efficiency and experimental practicality.

2.3 Two-stage baseline-free framework for damage identification

The overall process of the proposed two-stage baseline-free method is summarized as follows

Stage 1 — Damage localization using OFCRC:

1. Install acceleration sensors along the height of the wind turbine tower to collect response data under ambient or operational excitation.

2. Integrate acceleration signals and apply band-pass filtering to obtain displacement responses.
3. Compute fractional curvatures and construct the optimal fractional-order curvature ratio curve (OFCRC).
4. Identify damage locations by detecting abrupt changes in the OFCRC curve.

Stage 2 — Verification and quantification using FSM–IDSM:

1. Apply the optimal fractional-order statistical moment (FSM) method to extract accurate modal shapes from the same dataset.
2. Input the identified mode shapes into the improved direct stiffness method (IDSM) to estimate the bending stiffness of each tower segment.
3. Quantify the damage severity using the relative stiffness reduction.

The proposed method requires only a single measurement and no baseline data. The first stage (OFCRC) provides fast and sensitive damage localization, while the second stage (FSM–IDSM) validates and quantifies the damage extent. This combination ensures both efficiency and reliability in practical engineering applications for large wind turbine tower clusters. The detailed process is shown in Fig. 1.

To further assess the practical applicability of the proposed method, its computational efficiency and implementation feasibility are analyzed.

The overall computational procedure consists of three main steps:

1. Signal preprocessing, including mean removal, time-domain numerical integration, and zero-phase band-pass filtering of acceleration signals.
2. Fractional statistical moment (FSM) computation based on inter-story relative displacement.
3. Construction of the optimal fractional-order curvature ratio curve (OFCRC) for damage localization.

In the signal preprocessing stage, numerical integration is performed using a cumulative trapezoidal scheme in the time domain, while the band-pass filtering is implemented using a low-order Butterworth filter with zero-phase processing to avoid phase distortion. The FSM computation and OFCRC construction mainly involve vectorized algebraic operations, including absolute value, power, averaging, and ratio calculations.

As a result, the overall computational cost scales approximately linearly with the data size and does not involve iterative optimization, model updating, or training procedures. This ensures stable and efficient performance in practical applications.

It should be noted that the proposed method is intended for rapid and baseline-free structural damage screening rather than strict real-time monitoring. Nevertheless, the computational framework can be extended to near real-time applications through sliding-window processing and continuous data updating strategies.

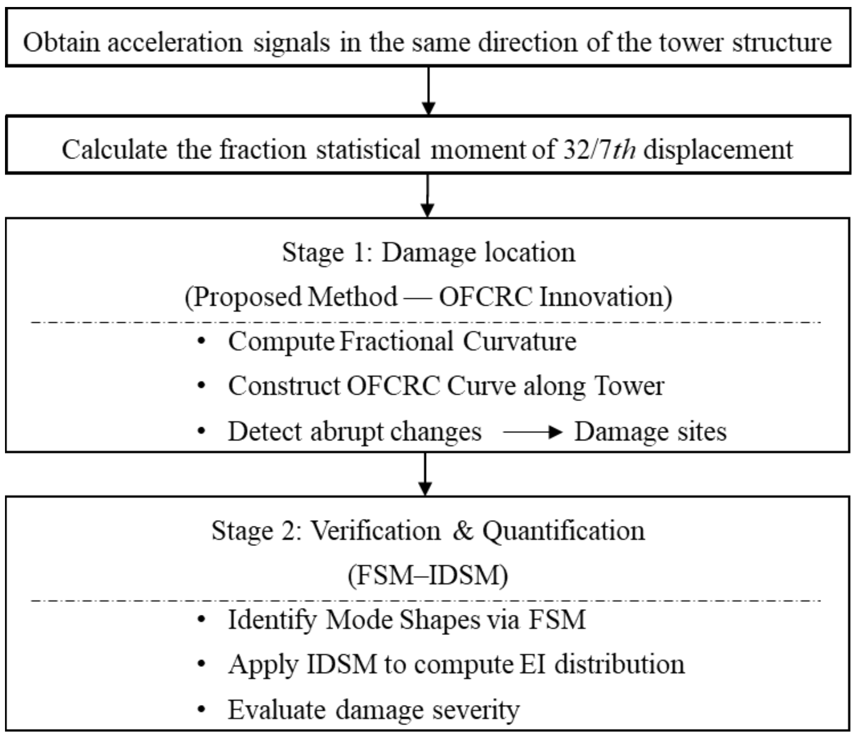

Fig. 1 Flow chart of the identification method

3. Numerical simulation

To validate the effectiveness and robustness of the proposed baseline-free two-stage method, numerical simulations were conducted using a representative 2 MW wind turbine tower. The model serve to verify both the localization capability of the proposed OFCRC and the quantitative accuracy of the subsequent FSM–IDSM verification stage. The tower has a height of 81.5 m, with bottom and top diameters of 4.1m and 2.5 m, respectively, and a wall thickness of 20 mm. The structural material properties are Q345D steel, with a Poisson's ratio of 0.3, a density of 7850 kg/m^3, and an elastic modulus of 210 GPa. To simplift the analysis, the upper mass of the structure is represented as a single mass point of 90 tons. The tower is evenly divided into 20 sections along its height for the simulatin. The schematic of the tower model is shown in Fig. 2. The two-stage method for damage identification will be simulated and validated.

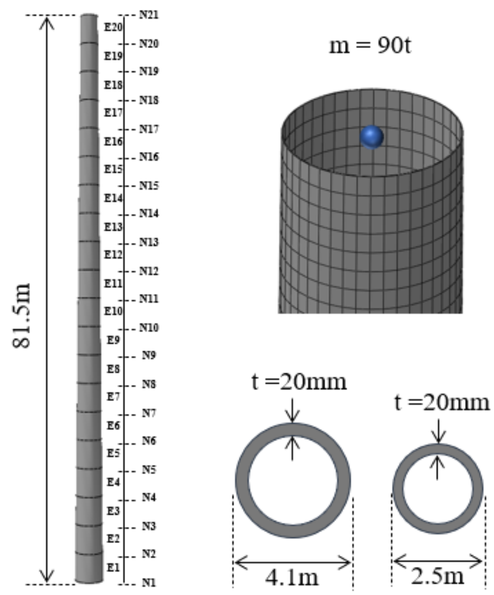

Fig. 2 Schematic of the tower model

3.1 Stage 1: Damage location identification via OFCRC

In the first stage, the OFCRC proposed in Section 2.1 is applied to identify damage locations. This baseline-free method only requires one on-site measurement and is characterized by rapid detection capabilities. Structural damage is simulated by reducing the stiffness of tower segments while accounting for environmental noise and varying form of external excitation. Applying noise with signal-to-noise ratios (SNR) of 40dB and 30dB on the structural response. White noise and EI centro waves were used as external incentive to verify the feasibility of the proposed method. The damage scenarios are: Case 1, non structural damage; Case 2, 10% stiffness reduction in Element 15; Case 3: 20% stiffness reduction in Element 11; and Case 4: 20% stiffness reduction in Elements 7 and 13. The detailed information is shown in Table 1.

Table 1 Working condition table

Detailed	Case	Excitation	SNR
Case 1: damage free	1-4	White noise, EI-Centro	Noise-free, 40 dB and 30 dB

Case 2: E15-10%	1-4	White noise, EI-Centro	Noise-free, 40 dB and 30 dB
Case 3: E11-20%	1-4	White noise, EI-Centro	Noise-free, 40 dB and 30 dB
Case 4: E7&E13-20%	1-4	White noise, EI-Centro	Noise-free, 40 dB and 30 dB

For each case, the OFCRC is constructed using the displacement responses obtained from the measured acceleration signals. The resulting curves for different SNRs under white-noise excitation are shown in Fig. 3, and the results under El Centro excitation are shown in Fig. 4.针对 Under noise-free conditions (Fig. 3a), the OFCRC of the undamaged structure (Case 1) shows a smooth, monotonic trend, indicating uniform stiffness distribution. For the damaged cases (Cases 2–4), distinct abrupt fluctuations appear at the corresponding element locations (E15, E11, E7 & E13), which precisely coincide with the predefined damage positions.

Even with noise levels of 40 dB and 30 dB (Fig. 3b–c), the OFCRC remains stable, and damage-induced peaks are still clearly distinguishable, demonstrating excellent noise immunity.

Similar results are observed under El Centro excitation (Fig. 4), further confirming the baseline-free and excitation-independent nature of the OFCRC-based localization approach.

These findings confirm that the OFCRC method can accurately localize damage using a single measurement, without requiring prior baseline data or multiple testing conditions.

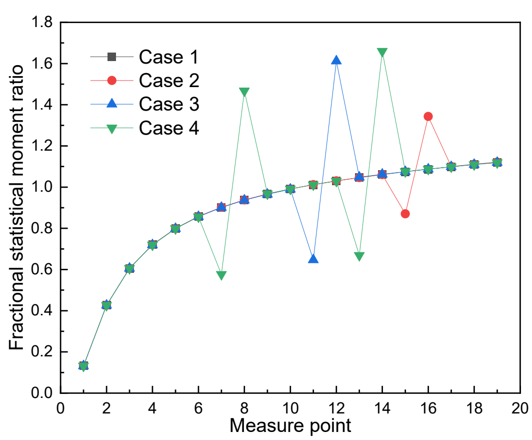

(a) Noiseless

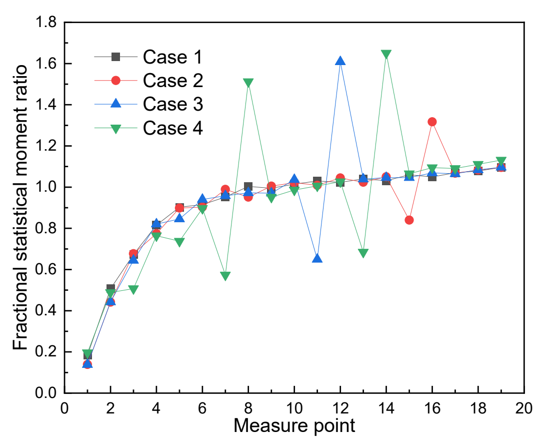

(b) 40dB

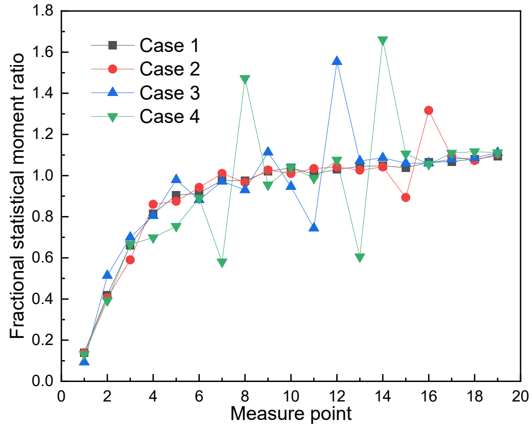

(c) 30dB

Fig. 3 Recognition results of different SNR under white noise excitation

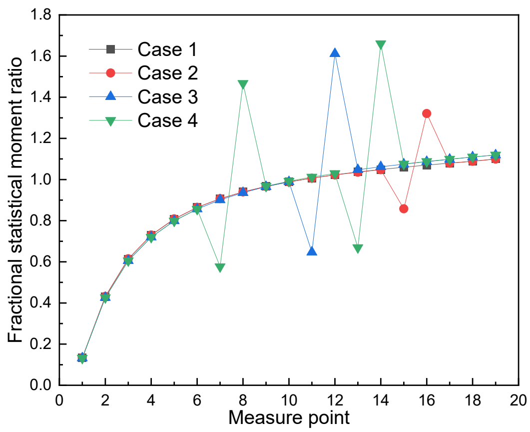

(a) Noiseless

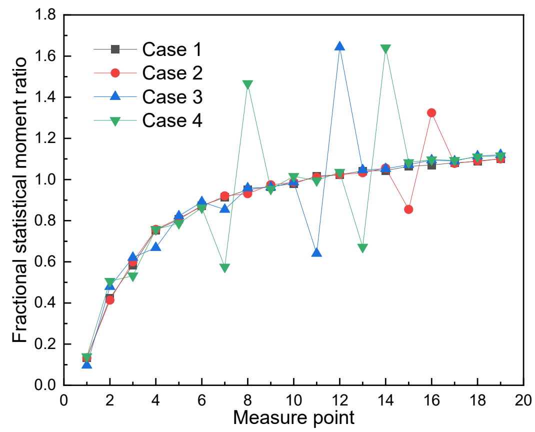

(b) 40dB

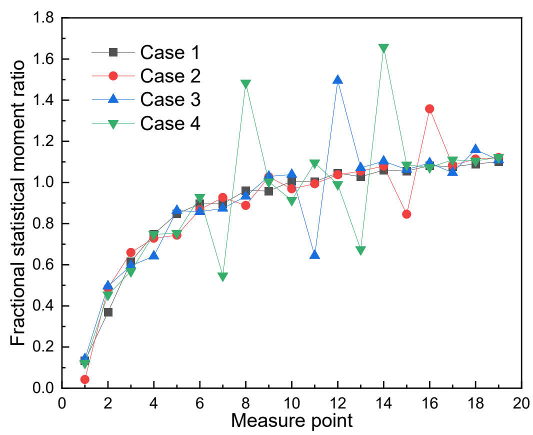

(c) 30dB

Fig. 4 Recognition results of different SNR under El-Centro excitation

To verify the effectiveness of the acceleration-reconstructed displacement for damage localization, a direct comparison of the OFCRC curves is conducted in the numerical simulation. Specifically, the OFCRC curves are calculated using two types of displacement signals: the directly simulated displacement (as the reference) and the displacement reconstructed from acceleration via double integration. Two representative damage cases under white-noise excitation are selected: Case 3 and Case 4. For both cases, the comparison is performed under the most unfavorable noise condition, i.e., SNR = 30 dB, as shown in Fig. 5.

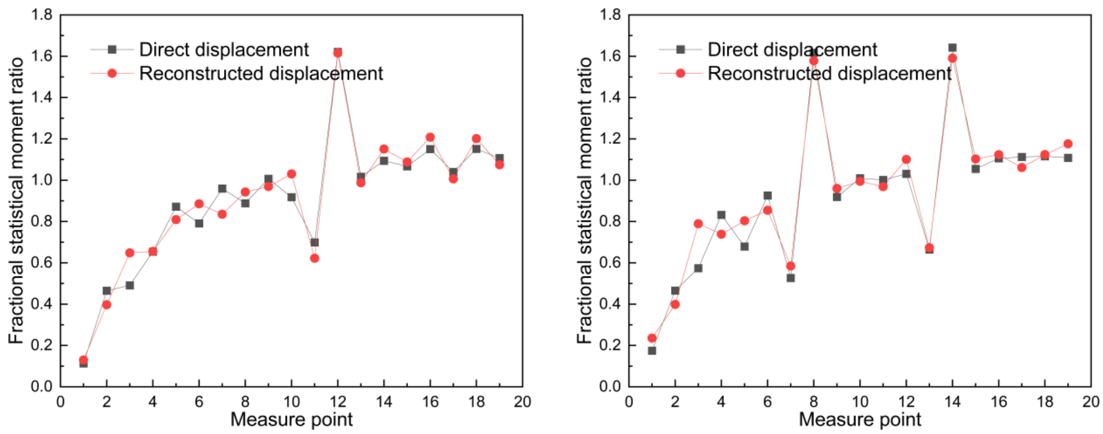

(a) Case3 (b) Case4

Fig. 5 Comparison of OFCRC curves based on direct and reconstructed displacement

The results demonstrate that, for both single-damage and multi-damage scenarios, the OFCRC curves derived from the reconstructed displacement exhibit clearly identifiable peaks at the same locations as those obtained from the directly simulated displacement. This confirms that the displacement reconstruction process introduces negligible influence on the damage localization capability, thereby validating the effectiveness of using acceleration-reconstructed displacement in the proposed method. More importantly, these results confirm that the OFCRC achieves accurate damage localization without any reliance on baseline data or extracted mode shapes. The indicator is computed exclusively from the ratios of relative displacement statistical moments between adjacent measuring points, demonstrating that it functions as a fully independent screening tool. The subsequent FSM – IDSM stage is only required for optional verification and severity quantification, not for localization itself.

3.2 Stage 2: Verification and Quantification Using FSM–IDSM

Following the identification of potential damage locations in Stage 1, Stage 2 aims to verify and quantify the severity of structural stiffness loss using the FSM–IDSM approach described in Section 2.2. First, the fundamental mode shape is identified using the FSM, and the modal assurance criterion (MAC) [1][44] is employed to compare the identified and theoretical mode shapes. The identified mode shapes are then used as inputs to the IDSM to compute nodal stiffness values. The identified mode shapes are then used as inputs to the IDSM to compute nodal stiffness values. The results for Cases 1–4 are shown in Figs. 6-9, and the quantitative stiffness errors are summarized in Table 2.

For the undamaged condition (Case 1), the stiffness distribution remains uniform, with a maximum error of only 2.7%. Fig. 6 shows the identification results of case 1 under different excitation and SNR conditions, where the structure is undamaged. Based on the identified vibration modes, the node stiffness identified using the IDSM is also consistent with the theoretical stiffness for the undamaged state, with a maximum error of only 2.74%, indicating that the structure is undamaged, aligning with the findings from the first stage of damage location identification.

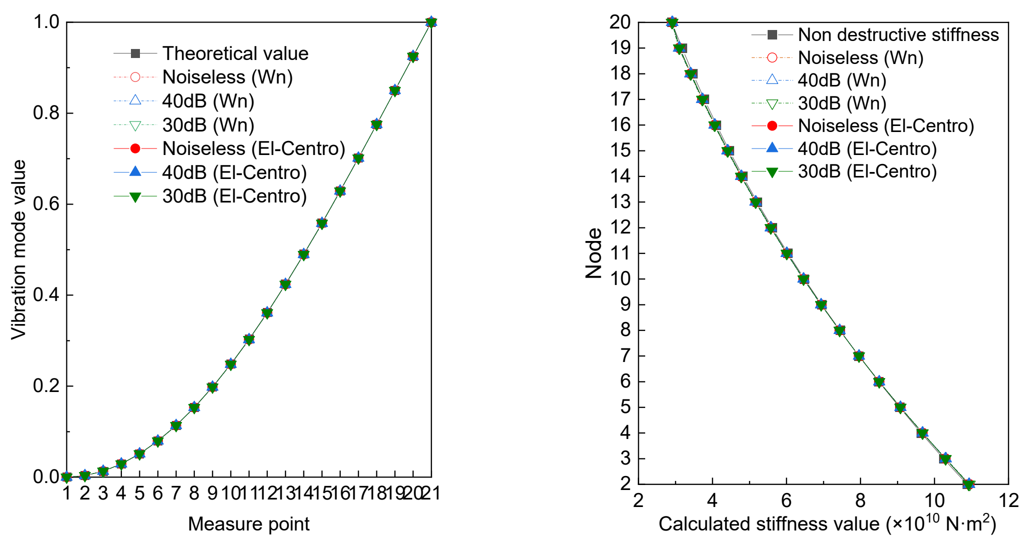

(a) Mode shape (b) Stiffness identification

Fig. 6 Identification results of case 1

For single-damage cases (Cases 2–3), localized stiffness reductions appear at the identified positions, with magnitude consistent with the simulated reduction (10–20%). Such as Fig. 7, shows the identification results of case 2 under different excitation and SNR conditions. In this case, a 10% decrease in the stiffness of element 15 results in a corresponding 5%. For instance, under El-Centro wave excitation with an SNR of 30dB, the stiffness at nodes 15 and 16 shows offsets of 6.03% and 5.88%, respectively.

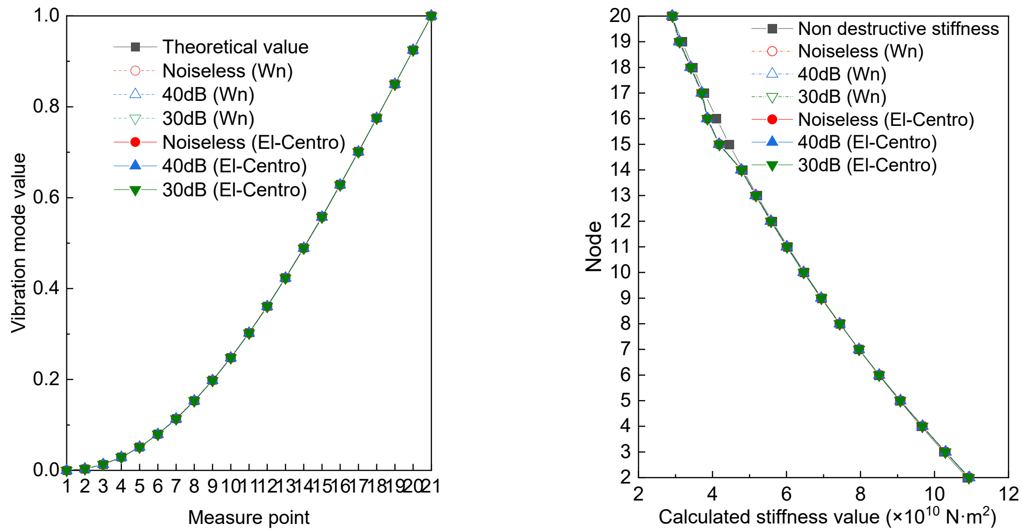

(a) Mode shape (b) Stiffness identification

Fig. 7 Identification results of case 2

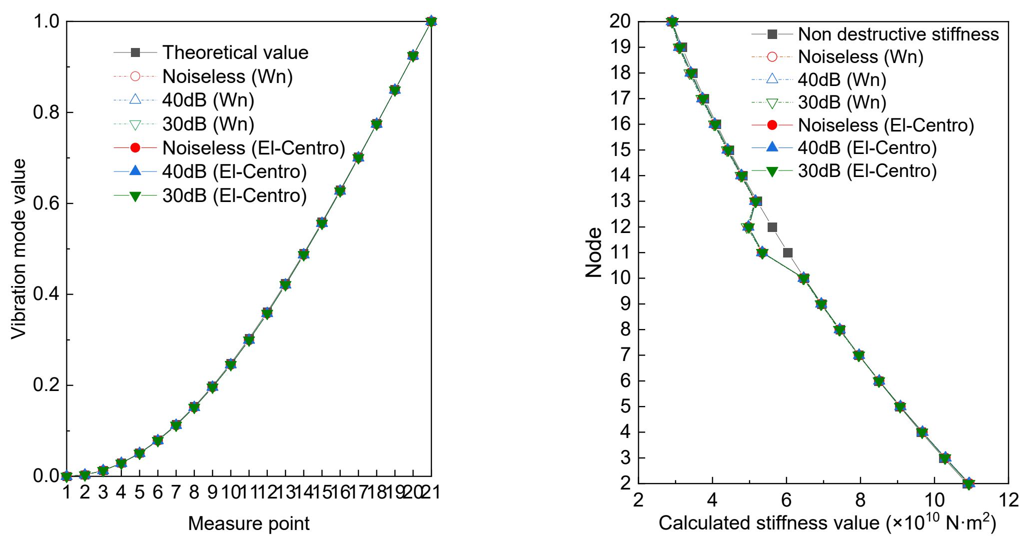

(a) Mode shape (b) Stiffness identification

Fig. 8 Identification results of case 3

For multiple-damage cases (Case 4), all damaged nodes show concurrent stiffness losses, confirming the accuracy of quantitative assessment.

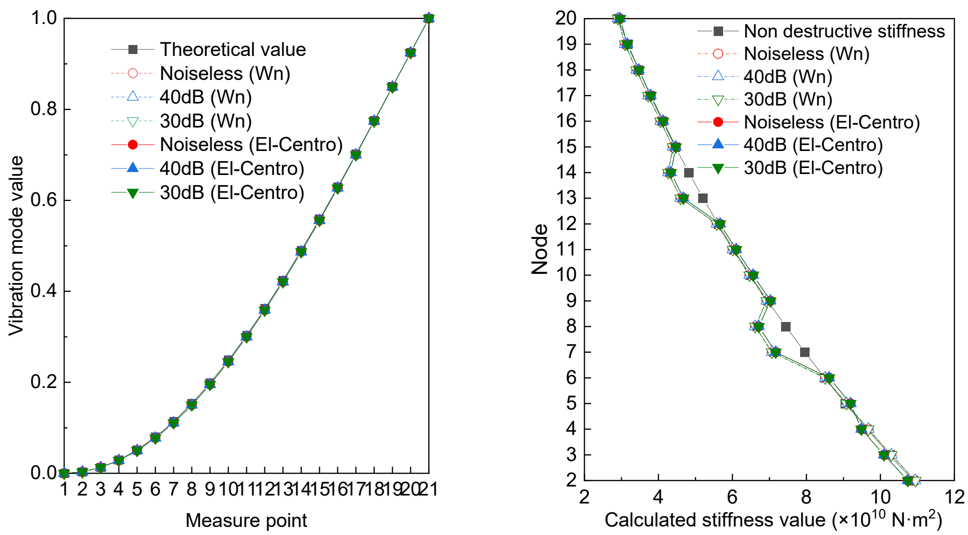

(a) Mode shape (b) Stiffness identification

Fig. 9 Identification results of case 4

In summary, the accurate identification of the fundamental vibration mode of the wind turbine tower structure provides favorable conditions for IDSM to identify the severity of structural damage. The damage severity identified in Stage 2 is consistent with the damage location identified in Stage 1. The proposed two-stage method demonstates strong noise resistance and delivers accurate results. Notably, it requires only a single on-site measurement, eliminating the need for initial values and significantly improving detection efficiency.

Table 2 (1-MAC) value under different cases ($\times 10^{-7}$)

	Whitenoise			El-centro		
	Noisefree	40dB	30dB	Noisefree	40dB	30dB
Case 1	7.62	9.37	9.40	5.50	5.80	6.65
Case 2	9.56	9.8	9.96	5.57	6.27	6.71
Case 3	9.48	10.00	16.5	5.62	5.63	5.92
Case 4	8.10	8.11	9.08	5.13	5.11	5.34

3.3 Robustness verification of underlying assumptions

3.3.1 Robustness to non-proportional damping

To evaluate the robustness of the proposed OFCRC-based damage localization method under realistic local damping variations caused by structural damage, a non-proportional damping analysis was conducted. In practical wind turbine towers, local damage or connection looseness can lead to increased energy dissipation, deviating from the ideal Rayleigh proportional damping assumption. In this analysis, the damping coefficients of the damaged story and its adjacent layers were locally amplified by a factor of 2.0 to simulate such effects. The excitation was white noise, and the signal processing and fractional statistical moment computation followed the same procedure as in Section 3.1, with measurement noise levels of 40 dB and 30 dB. The resulting OFCRC curves are shown in Fig. 10.

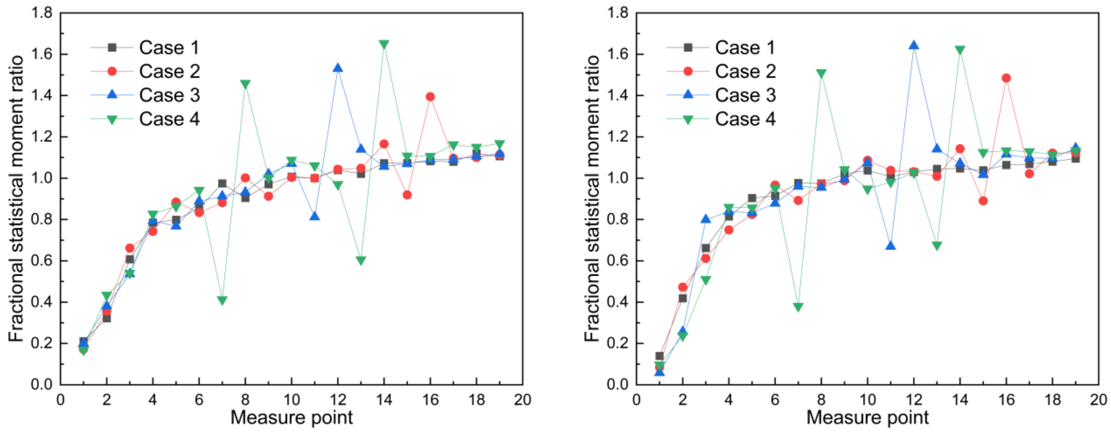

(a) 40dB (b) 30dB

Fig. 10 Recognition results under non-proportional damping

The resulting OFCRC curves indicate that sharp peaks consistently appear at the locations of structural damage in all scenarios. The locally increased damping introduces minor undulations in the curves, but these variations are gradual and clearly distinguishable from the abrupt peaks caused by stiffness reduction, leaving the damage-sensitive indicators unaltered. Even at 30 dB, the damage-induced peaks remain clearly identifiable.

These results demonstrate that localized non-proportional damping caused by structural damage does not compromise the OFCRC's ability to accurately identify stiffness reductions. The fundamental mode curvature of lightly damped steel towers is primarily governed by the stiffness distribution, whereas local damping anomalies only affect higher-order effects, which cannot override the dominant curvature discontinuities caused by stiffness loss. Therefore, the Rayleigh damping assumption employed in the theoretical derivation is considered appropriate for the intended application.

3.3.2 Robustness to weak base restraint

To evaluate the robustness of the proposed OFCRC-based damage localization method under realistic boundary nonlinearity at the tower base, a weak restraint analysis was conducted. In actual wind turbine towers, boundary nonlinearity can arise from bolt relaxation or contact micro-slip at the base flange, which may occur even under small-amplitude operational vibrations and cause the base restraint to deviate from the ideally fixed condition. In this analysis, a grounding spring was introduced at the bottom node in the horizontal direction, with its stiffness set to $k_{spring} = 1\times10^{10}$ N/m. This value substantially exceeds the bending stiffness of the lowest story, ensuring that the fundamental mode remains an elastic bending mode, while being clearly below the infinite rigidity of a perfectly fixed base. The excitation was white noise, and the signal processing and fractional statistical moment computation followed the same procedure as in Section 3.1, with measurement noise levels of 40 dB and 30 dB. The resulting OFCRC curves are shown in Fig. 11.

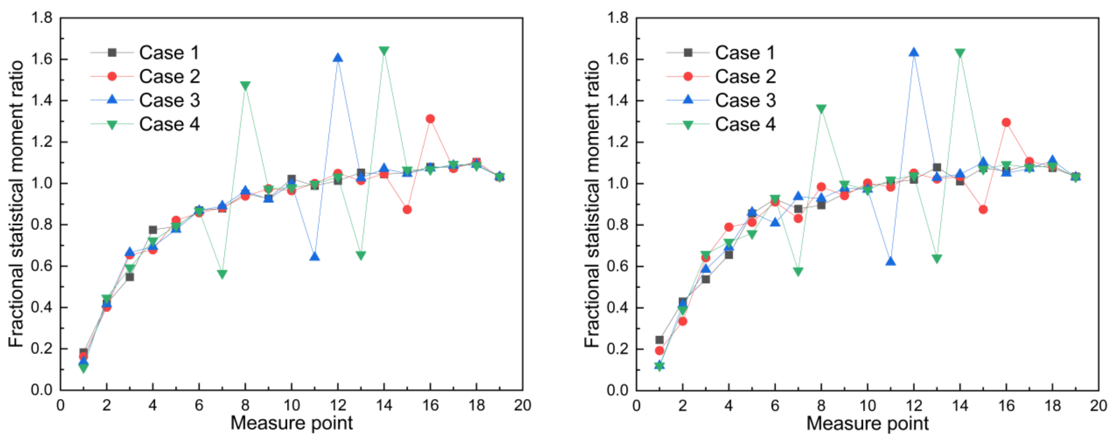

(a) 40dB (b) 30dB

Fig. 11 Recognition results under weak base restraint

The resulting OFCRC curves indicate that sharp peaks consistently appear at the locations of structural damage in all scenarios. The weak base restraint introduces a gradual tilting of the curve near the bottom end, but this variation is smooth in character and clearly distinguishable from the abrupt peaks caused by stiffness reduction. Consequently, the damage-sensitive indicators remain unaltered. Even at 30 dB, the damage-induced peaks remain clearly identifiable.

These results demonstrate that a moderate relaxation of the base fixity does not compromise the OFCRC's ability to accurately identify stiffness reductions. The fundamental mode curvature of the tower is primarily governed by the stiffness distribution along the height, and the boundary flexibility only alters the overall normalization of the mode shape, which is largely eliminated by the curvature ratio operation. Therefore, the linear structural behavior assumption adopted in the theoretical derivation is considered appropriate for the intended application.

4. Scaled model test

To verify the applicability of the proposed damage identification method for wind turbine towers under local stiffness degradation conditions, a scaled model test of a wind turbine tower was conducted. The prototype was a 72 m high in-service wind turbine tower. According to the dynamic similarity theory, a geometric scaling ratio of 3:40 was adopted to construct the scaled model. The model mainly consisted of the tower body, flange connections, a rigid foundation, and simplified blade auxiliary structures. The overall structural configuration strictly followed the prototype tower design to ensure similarity in dynamic characteristics and vibration transmission paths.

The tower body was fabricated from Q345 steel plates through precision rolling and discretized along the height into a three-segment structure connected by flange plates to preserve the connection characteristics of the actual tower. The heights of the three tower segments were 1750 mm, 1850 mm, and 1850 mm, respectively. The wall thickness was 6 mm, with an elastic modulus of 210 GPa, a Poisson's ratio of 0.3, and a density of 7850 kg/m³. As the key damage-sensitive locations, the flange connections were assembled using M12 × 70 high-strength bolts. Local stiffness degradation damage was simulated by loosening two adjacent bolts at the third-level flange. This damage type is consistent with the commonly observed flange connection loosening in practical engineering and represents a typical local stiffness degradation condition. Although its influence on the global structural response is limited, it possesses strong engineering representativeness. The bottom of the model adopted a rigid foundation composed of thick steel plates and H-shaped steel to ensure fixed-end boundary conditions. The top of the model was equipped with upper connection components and blade-like auxiliary structures to maintain the rationality of the tower-top structural configuration, installation path, and overall external mass distribution.

Considering the sensor installation conditions, the number of acquisition interfaces, and cable layout length, five acceleration sensors were arranged along the tower height to obtain synchronous dynamic responses of the structure. The sensors were installed above each flange level and at the foundation location, with a sampling frequency of 100 Hz. The test included two conditions: a healthy condition (all bolts tightened with pretension) and a damaged condition (two bolts loosened at the third-level flange). Manual pulse excitation was applied at the tower base, and acceleration signals were collected. The sensor installation details and scaled model test setup are shown in Fig. 12. The acceleration data collected under the two conditions are shown in Fig. 13.

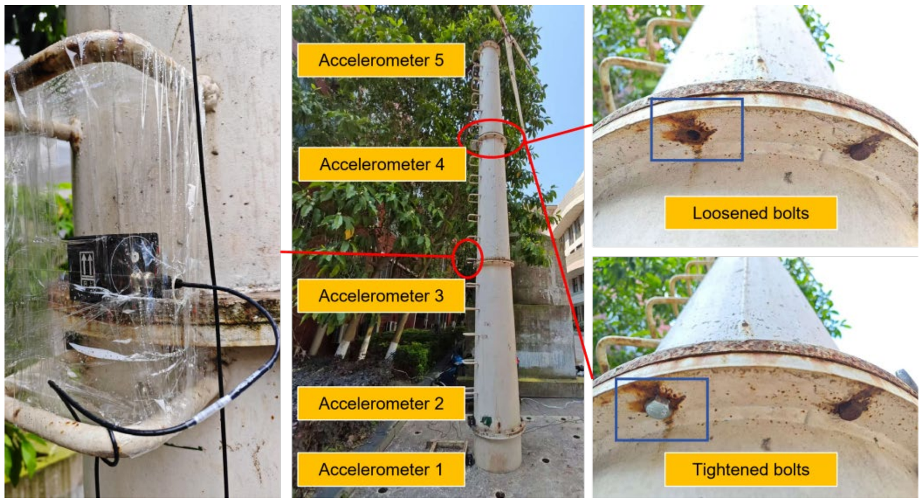

Fig. 12 Scaled test details

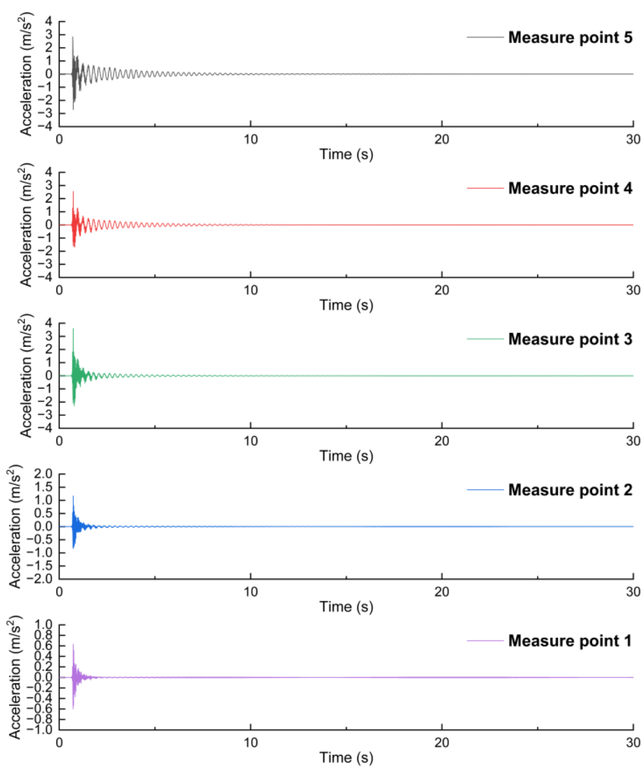

(a) Time-history signal of health condition scale model

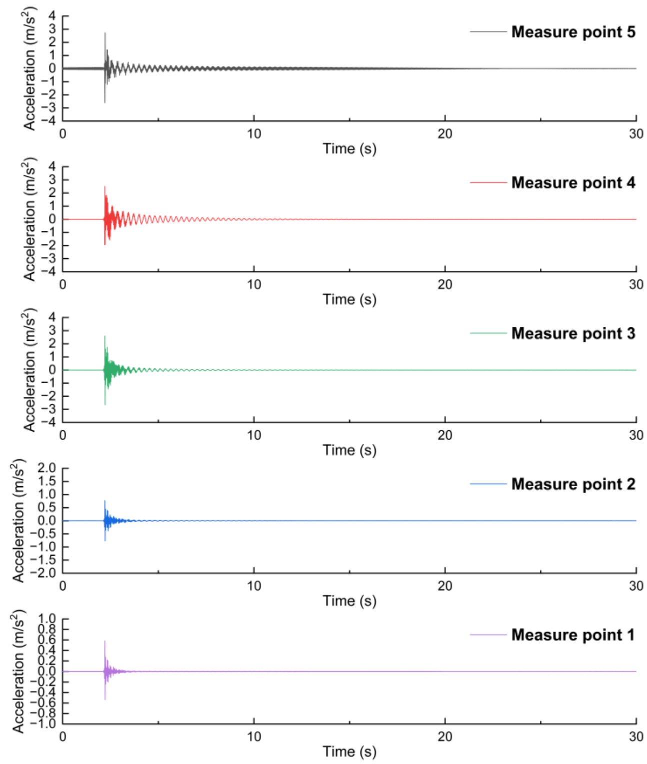

(b) Time-history signal of damage condition scale model

Fig. 13 Time-history signal

By applying a fast Fourier transform to the collected acceleration response signals, the first-order natural frequency at different heights was identified as 3.6 Hz. Subsequently, the two-stage framework proposed in this study was employed for damage identification of the tower model. In the first stage, the OFCRC method was adopted for local stiffness degradation localization analysis, as shown in Fig. 14. Under the healthy condition, the OFCRC curve exhibited a smooth and continuous increasing trend along the tower height without noticeable abrupt changes, indicating that the global stiffness distribution of the structure was continuous and free of local anomalies. In contrast, under the damaged condition, the OFCRC curve showed obvious deviations in the upper adjacent segments of the tower, reflecting the characteristics of local stiffness degradation. Since only five measurement points were arranged in the test, four OFCRC curve points were formed correspondingly. The loosening of flange bolts may simultaneously affect adjacent segments, resulting in abnormal variations in the upper neighboring segments. Although the number of measurement points was limited, the anomalous regions identified by OFCRC were generally consistent with the predefined locations of loosened flange bolts, indicating that the proposed method could still effectively reflect local stiffness degradation characteristics under limited measurement conditions.

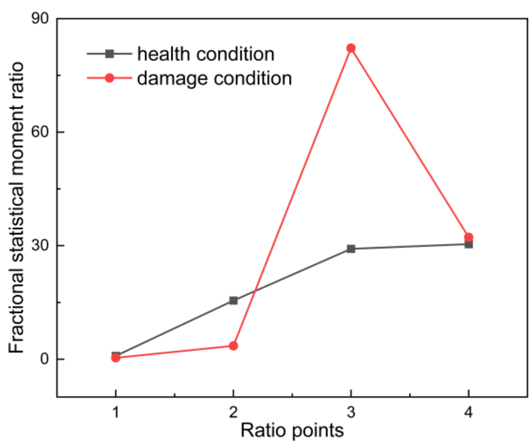

Fig. 14 OFCRC results under healthy and damaged conditions

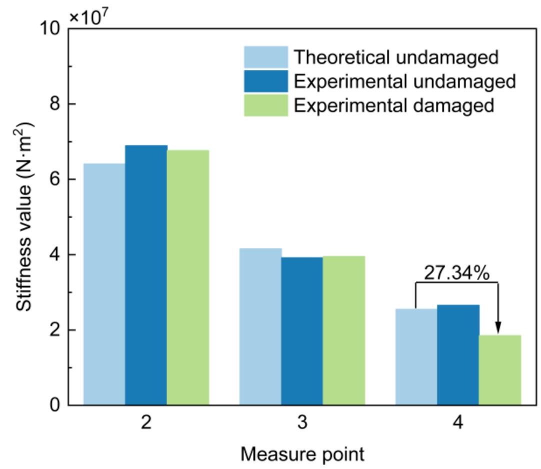

Fig. 15 Scaled model stiffness identification

After the preliminary localization of the damage position, the FSM-IDSM method was further employed in the second stage to quantitatively evaluate the structural stiffness, as shown in Fig. 15. The results indicate that the stiffness at the measurement points near the loosened bolts decreased significantly, with a maximum stiffness reduction of 27.34%. The theoretical undamaged stiffness values were generally in good agreement with the experimentally identified undamaged stiffness values, with a maximum error of 7.54%. The stiffness degradation locations were basically consistent with the anomalous regions identified by OFCRC, further verifying the effectiveness and feasibility of the proposed method for local connection damage identification and stiffness quantification.

In addition to the identification accuracy, the computational efficiency of the proposed method was evaluated based on the experimental data processing procedure. The complete workflow, including signal preprocessing (mean removal, time-domain numerical integration, and zero-phase band-pass filtering), fractional statistical moment (FSM) computation, and OFCRC construction, was implemented in MATLAB. For the measured dataset consisting of 5 measurement points and 3000 sampling points, the total processing time was approximately 4.09 seconds on a standard desktop computer. The computational time is mainly dominated by the signal preprocessing stage, particularly the numerical integration and filtering operations, while the FSM computation and OFCRC construction contribute only marginally due to their non-iterative and vectorized nature.

These results demonstrate that the proposed method can achieve rapid structural damage screening with relatively low computational cost, supporting its practical applicability in engineering scenarios.

5. Onsite test

The on-site experiment was conducted at a wind farm in Chongqing, focusing on the 24th wind turbine tower. This tower has a height of 87m and consists of 5 tubulars. Considering the working platform setup inside the tower, sensor installation conditions, the number of data acquisition instrument interfaces, and the length of the data acquisition cables, five acceleration sensors were used for synchronous signal acquisition. The data acquisition device and computer were installed on the working platform near the flange at the connection between the third and fourth tower sections. The sensors were installed at heights of 3m, 24m, 43m, 64m, and 85m, respectively, to capture the acceleration response of the tower body in the same horizontal direction. During the experimental measurement process, external wind forces were relatively low, and the blades were stationary, and the wind turbine tower was in a shutdown state. The tower, newly built and meeting engineering quality acceptance standards, had already passed inspections, as shown in Fig. 16. The sampling frequency was set at 100Hz, and the collected acceleration responses are shown in Fig. 17.

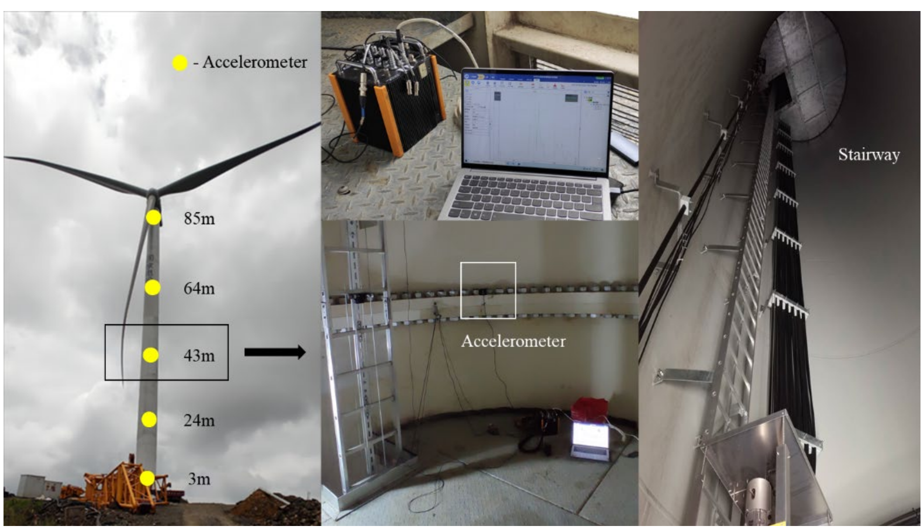

Fig. 16 Numerical model

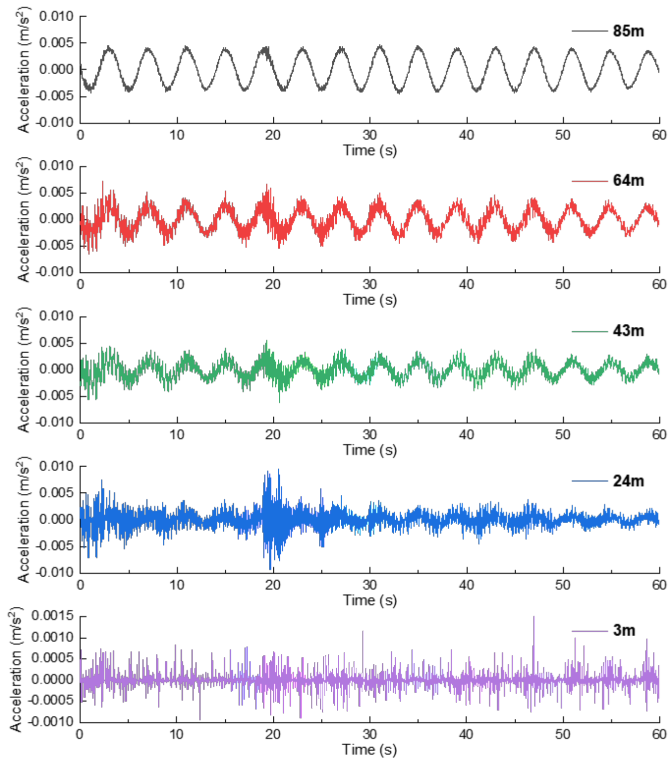

Fig. 17 Acceleration response signal

The first-order frequency of the data at different heights can be obtained as 0.26Hz by performing a fast Fourier transform to the collected acceleration response signals. Subsequently, the acceleration signal is integrated to obtain the displacement signal, and the first-order response signal is retained using bandpass filtering to calculate the FSM.

Firstly, using stage 1 method, the location of the damage is identified based on the OFCRC, and the identification results are shown in Fig. 18. The ratio curve shows an increasing trend with the height of the wind turbine tower without any noticeable abrupt changes, indicating that the structure has not undergone any sudden stiffness changes. The wind power tower has recently been constructed and has not yet entered formal operation. However, it has passed quality inspections and is ready for grid-connected power generation in the next phase. These results indicate the feasibility of the stage 1 method for preliminarily determining the location of damage in wind turbine tower structures.

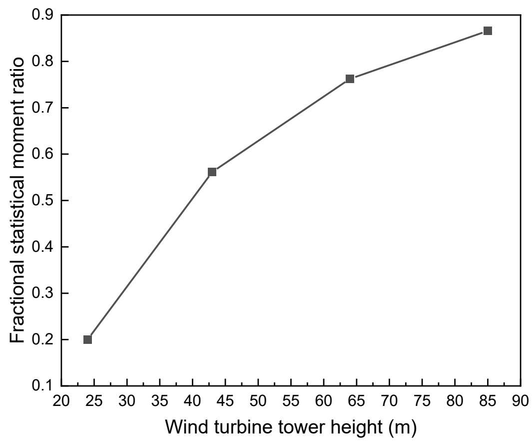

Fig. 18 FSM ratio curve

Next, the stage 2 method is used to identify damage severity of the wind turbine tower structure. The first-order modal shape of the tower is identified using the FSM, and then the severity of structural damage is identified through an improved direct stiffness method. The results are consistent with and verified by the stage 1 method. The identification results are shown in Fig. 19. By substituting the identified first-order modal shape values into the improved direct stiffness method, the stiffness values at the measurement heights of 24m, 43m, and 64m are calculated. The maximum error compared to the theoretical stiffness values is only 5.4%, indicating that no damage has occurred to in these sections of the tower. Furthermore, no sudden changes in stiffness values are observed at the heights of 24m and 64m, confirming that the adjacent measuring points (3m and 85m) are also undamaged.

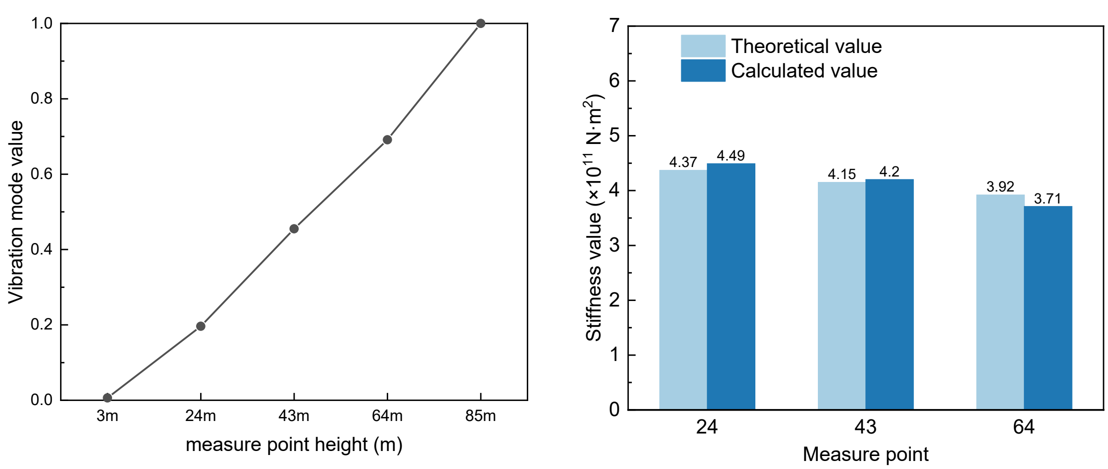

(a) Mode shape (b) Stiffness identification

Fig. 19 Identification of vibration mode and damage severity

6. Conclusions and extensions

This study proposed a baseline-free two-stage framework for structural damage identification in wind turbine towers, combining the optimal fractional-order curvature ratio curve (OFCRC) with the FSM-based modal identification and improved direct stiffness method (FSM–IDSM). The main conclusions and contributions can be summarized as follows.

(1) Innovation in baseline-free damage localization. A novel fractional-order curvature ratio curve (OFCRC) was derived, which is formulated directly from the ratios of relative displacement statistical moments between adjacent measuring points, requiring neither modal identification nor baseline records. Numerical simulations, scaled-model tower experiments, and onsite tests demonstrated that the OFCRC can accurately localize structural damage without requiring baseline information, even under strong measurement noise and varying excitation conditions. This self-contained nature constitutes the core methodological innovation of this study, enabling truly single-measurement damage localization for practical tower-type structures.

(2) Verification and quantitative assessment using existing FSM–IDSM theory. Building upon previously validated methods, the FSM-based modal identification and improved direct stiffness method were integrated as a verification and quantification module. The combined FSM–IDSM results exhibited excellent agreement with simulated and experimental data, successfully quantifying the stiffness loss identified by the OFCRC stage. This confirms the accuracy, consistency, and engineering interpretability of the proposed framework.

(3) Engineering applicability and future extensions. The proposed OFCRC–FSM–IDSM framework provides a complete and baseline-free solution for rapid damage localization and quantitative assessment of wind turbine towers under ambient excitation. The methodology can be extended to other large-scale civil structures such as bridge piers, offshore platforms, and transmission towers.

Overall, this study establishes a practical and theoretically sound approach that bridges the gap between fractional-order theory and structural health monitoring applications, providing a new paradigm for baseline-free, noise-robust, and efficient damage detection in engineering practice. Despite the promising results, the current study is limited by the field validation on only an undamaged tower. Future work should include controlled damage experiments and extend the method to a wider range of operational and environmental conditions. Additionally, the influence of sensor density and placement on detection accuracy warrants further investigation.

CRediT authorship contribution statement

Yuanqing Fan: Writing – review & editing, Writing – original draft. **Yang Yang**: Review & editing, Supervision, Funding acquisition, Methodology, Conceptualization.. **Zhewei Wang**: Writing – original draft. **Giuseppe Lacidogna**: Validation, Investigation, Formal analysis. **Jie Luo**: Writing – review & editing. **Jiaji Wang**: Writing – Resources, Project administration.

Acknowledgments

We are grateful to the following agencies for their support toward this study: Research Project of Zhejiang Provincial Department of Transportation-Intelligent Detection Method for Mechanical Indicators of Bridge Structures(2025016);Guizhou Province Academician Workstation for Research and Application of Intelligent Equipment Technology in Civil Engineering(Qiankehe Platform KXJZ (2025) 004).

Reference

[1] Jiang, T., Lv, P., & Li, D. (2024). A new shape reconstruction method for monitoring the large deformations of offshore wind turbine towers. *Ocean Engineering*, *312*, 119253.

[2] Chen, J., Zhang, M., Zhu, H., Xu, F., Shao, Z., Ding, F., & Xiang, P. (2024). Study on mechanical properties of wind turbine tower reinforced by ribbed interlayer. *Journal of Constructional Steel Research*, *212*, 108256.

[3] Moynihan, B., Mehrjoo, A., Moaveni, B., McAdam, R., Rüdinger, F., & Hines, E. (2023). System identification and finite element model updating of a 6 MW offshore wind turbine using vibrational response measurements. *Renewable Energy*, *219*, 119430.

[4] Duan, L. X., Wang, W. D., Zheng, L., & Shi, Y. L. (2024). Dynamic response analysis of monopile CFDST wind turbine tower system under wind-wave-seismic coupling action. *Thin-Walled Structures*, 112089.

[5] Zhang, D., Bhattarai, H. B., Wang, F., Zhang, X., Hwang, H. J., Wu, X., ... & Kang, S. (2024). Dynamic characteristics of segmental assembled HH120 wind turbine tower. *Engineering Structures*, *303*, 117438.

[6] Cadoret, A., Denimal-Goy, E., Leroy, J. M., Pfister, J. L., & Mevel, L. (2025). Damage detection and localization method for wind turbine rotor based on Operational Modal Analysis and anisotropy tracking. *Mechanical Systems and Signal Processing*, *224*, 111982.

[7] Serrano-Antoñanazas, M., Sierra-Garcia, J. E., Santos, M., & Tomas-Rodríguez, M. (2023). Identification of Vibration Modes in Floating Offshore Wind Turbines. *Journal of Marine Science and Engineering*, *11*(10), 1893.

[8] Xi, Y., Li, H., Sun, L., & Wang, Z. (2024). Extreme load extrapolation and long-term fatigue assessment of offshore wind turbine tower based on monitoring data. *Ocean Engineering*, *300*,

117180.

[9] Zhao, Y., Li, X., Wang, X., Jiang, J., & Wang, Z. (2023). Fatigue Life Evaluation of Wind Turbine Tower Based on Measured Data. *Advances in Civil Engineering*, *2023*(1), 1100725.

[10] Lin, L., Zhang, X., Zhang, D., Wu, X., Liu, Y., Wang, X., ... & Yang, T. (2023). Damage evolution and failure analysis of the advanced transition segment behavior of wind turbine tower. *Engineering Failure Analysis*, *152*, 107527.

[11] Shamir, M., Braithwaite, J., & Mehmanparast, A. (2023). Fatigue life assessment of offshore wind support structures in the presence of corrosion pits. *Marine Structures*, *92*, 103505.

[12] Yao, Q., Bing, H., Zhu, G., Xiang, L., & Hu, A. (2024). A novel stochastic process diffusion model for wind turbines condition monitoring and fault identification with multi-parameter information fusion. *Mechanical Systems and Signal Processing*, *214*, 111397.

[13] Lin, K., Ma, B., Yang, S., & Zhou, A. (2024). Experimental study of wind turbine in operation under wind and seismic excitations with soil-structure interaction. *Engineering Structures*, *308*, 117927.

[14] Simoncelli, M., Zucca, M., & Ghilardi, M. (2024). Structural health monitoring of an onshore steel wind turbine. *Journal of Civil Structural Health Monitoring*, 1-15.

[15] Yang, Y., Hossen, M. S., Lacidogna, G., Xu, W., Kawsar, I., Sun, J., & Hossain, S. (2025). Effect of temperature on the modal parameters of continuous rigid frame bridge. *Developments in the Built Environment*, *21*, 100631.

[16] Pacheco, J., Pimenta, F., Pereira, S., Cunha, Á., & Magalhães, F. (2022). Fatigue assessment of wind turbine towers: Review of processing strategies with illustrative case study. *Energies*, *15*(13), 4782.

[17] Yang, Y., Liang, F., Zhu, Q., & Zhang, H. (2024). An Overview on Structural Health Monitoring and Fault Diagnosis of Offshore Wind Turbine Support Structures. *Journal of Marine Science and Engineering*, *12*(3), 377.

[18] Ye, Z., Lovell, L., Faramarzi, A., & Ninić, J. (2024). Sam-based instance segmentation models for the automation of structural damage detection. *Advanced Engineering Informatics*, *62*, 102826.

[19] Wang, P. G., Bai, Y., Wang, M., Zhao, M., & Du, X. L. (2024). Seismic vulnerability and performance-based assessment of monopile offshore wind turbine considering turbine blades. *Soil Dynamics and Earthquake Engineering*, *186*, 108918.

[20] Zheng, Y., Gao, Y., Lu, S., & Mosalam, K. M. (2022). Multistage semisupervised active learning framework for crack identification, segmentation, and measurement of bridges. *Computer-Aided Civil and Infrastructure Engineering*, *37*(9), 1089-1108.

[21] Yuan, X., Huang, Q., Song, D., Xia, E., Xiao, Z., Yang, J., ... & Joo, Y. H. (2024). Fatigue Load Modeling of Floating Wind Turbines Based on Vine Copula Theory and Machine Learning. *Journal of Marine Science and Engineering*, *12*(8), 1275.

[22] Ren, C., & Xing, Y. (2024). An efficient active learning Kriging approach for expected fatigue damage assessment applied to wind turbine structures. *Ocean Engineering*, *305*, 118034.

[23] Guo, J., Ji, X., Song, H., Chang, S., & Liu, F. (2022). Unsupervised statistical estimation of offshore wind turbine vibration for structural damage detection under varying environmental conditions. *Engineering Structures*, *272*, 115005.

[24] Xiong, C., Dai, K., Luo, Y., Yang, Z., Qiu, K., & Tang, X. (2024). Proposal and application of onshore lattice wind turbine support structure and integrated multi-scale fatigue assessment method. *Engineering Structures*, *302*, 117314.

[25] Li, S. Z., Zhou, X. H., Gao, Y., Wang, Y. H., Gan, D., Ren, W., ... & Zhu, R. H. (2023). Damage detection of concrete segment in steel-concrete hybrid wind turbine tower. *Structures*, *56*, 105009.

[26] Bai, H., Shi, L., Aoues, Y., Huang, C., & Lemosse, D. (2023). Estimation of probability distribution of long-term fatigue damage on wind turbine tower using residual neural network. *Mechanical Systems and Signal Processing*, *190*, 110101.

[27] Zhang, Z., Sun, C., & Jahangiri, V. (2022). Structural damage identification of offshore wind turbines: A two-step strategy via FE model updating. *Structural Control and Health Monitoring*, *29*(2), e2872.

[28] Hubbard, P. G., Xu, J., Zhang, S., Dejong, M., Luo, L., Soga, K., ... & Minto, C. (2021). Dynamic structural health monitoring of a model wind turbine tower using distributed acoustic sensing (DAS). *Journal of civil structural health monitoring*, *11*(3), 833-849.

[29] Motlagh, M. M., Bahar, A., & Bahar, O. (2021). Damage detection in a 3D wind turbine tower by using extensive multilevel 2D wavelet decomposition and heat map, including soil-structure interaction. *Structures*, *31*, 842-861.

[30] Wong, C. N., Chen, J. C., & To, W. M. (1996). Eigenparameter perturbation method for structural damage detection. P*roceedings of the AIAA/ASME/AHS Adaptive Structures Forum*, 18–19 April, Salt Lake City, USA.

[31] Wong, C. N., Zhu, W. D., & Xu, G. Y. (2004). On an iterative general-order perturbation method for multiple structural damage detection. *Journal of Sound and Vibration*, 273(1–2), 363–386.

[32] Wong, C. N., & Barhorst, A. A. (2009). General-order perturbation with a skew-symmetric approach for structural health monitoring of a modular beam. *Journal of Vibration and Control*, 15(12), 1783–1807.

[33] Bhowmik, B., Tripura, T., Hazra, B., & Pakrashi, V. (2019). First-order eigen-perturbation techniques for real-time damage detection of vibrating systems: Theory and applications. *Applied Mechanics Reviews*, 71(6), 060801.

[34] Ulriksen, M. D., Greś, S., & Bernal, D. (2024). Perturbation-invariant eigenvalue assignment for statistical damage localization. *Journal of Physics: Conference Series*, 2647, 192017.

[35] Li, J. H., Yang, Q. W., Shen, X., & Liang, C. F. (2013). Structural damage diagnosis using an improved eigenvalue perturbation method. *Advanced Materials Research*, 753–755, 2347–2350.

[36] Oh, S. Y., Joung, C., Lee, S., Shim, Y. B., Lee, D., Cho, G. E., ... & Park, Y. B. (2024). Condition-based maintenance of wind turbine structures: A state-of-the-art review. *Renewable and Sustainable Energy Reviews*, *204*, 114799.

[37] Yang, Y., Wang, Z., Yang, Q., Tan, X., & Gao, Y. (2024). Bridge bearing damage identification based on statistical moment change rate. *Mechanical Systems and Signal Processing*, *206*, 110898.

[38] Yang, Y., Ling, Y., Tan, X. K., Wang, S., & Wang, R. Q. (2022). Damage identification of

frame structure based on approximate Metropolis–Hastings algorithm and probability density evolution method. *International Journal of Structural Stability and Dynamics*, *22*(03n04), 2240014.
[39] Yang, Y., Wang, Z., Tao, S., Yang, Q., & Chai, H. K. (2024). Modal identification of wind turbine tower based on optimal fractional order statistical moments. *Computer-Aided Civil and Infrastructure Engineering*.
[40] Yang, Y., Lu, H., Tan, X., Chai, H. K., Wang, R., & Zhang, Y. (2022). Fundamental mode shape estimation and element stiffness evaluation of girder bridges by using passing tractor-trailers. *Mechanical Systems and Signal Processing*, *169*, 108746.
[41] Clough, R.W., et al. (1995). Dynamics of Structures. USA, Computers & Structures, Inc., Berkeley, CA, 326-328.
[42] Yang, Y., Lu, H., Tan, X., Wang, R., & Zhang, Y. (2022). Mode shape identification and damage detection of bridge by movable sensory system. *IEEE Transactions on Intelligent Transportation Systems*, *24*(1), 1299-1313.
[43] Yang, Y., Tan, X., Lu, H., Xue, S., Wang, R., & Zhang, Y. (2022). Indirect approach to identify girder bridge element stiffness based on blind source separation. *Symmetry*, *14*(10), 1963.
[44] Greś, S., Döhler, M., & Mevel, L. (2021). Uncertainty quantification of the modal assurance criterion in operational modal analysis. *Mechanical Systems and Signal Processing*, *152*, 107457.